Available online at www.sciencedirect.com
SCIENCE DIRECT®
Journal of Magnetic Resonance 175 (2005) 114–123
JMR Journal of Magnetic Resonance
www.elsevier.com/locate/jmr

Computing the $\mathbf{B}_1$ field of the toroidal MRI coil

Edward J. Butterworth *, John C. Gore

Vanderbilt University Institute of Imaging Sciences, CCC 1121 MCN, Nashville, TN 37232-2675, USA

Received 20 July 2004; revised 3 March 2005

Abstract

We present an analytic solution for the B_1 field produced in a gapped toroidal cavity resonator designed as a probe for high field MRI. This resonator supports standing TEM waves, so its electric and magnetic fields are identical to those produced by a stationary planar current source with the same (constant) cross-section multiplied by a complex exponential propagation factor. An explicit expression for the field may therefore be found by solving Laplace's equation for the static potential, which is accomplished with a two-dimensional logarithmic conformal transformation algorithm. The equipotential curves are also the contours of the field strength B, and the $\mathbf{B}$ (vector) field at any point is directed along the contour passing through that point. With this information, we construct the solution by computing the angle made by the equipotential curve with the horizontal axis at each point, using this angle to analyze the B field into its x and y components, and adding the contributions from the current sources to obtain the magnitude and direction of B at each point in the region of interest. Some proposed extensions of this algorithm are also discussed.

Keywords: Electromagnetic field mapping; Conformal mapping; MRI RF coil modeling; Analytic solutions; RF design

1. Introduction

Image quality in MRI depends sensitively on $\mathbf{B}_1$ homogeneity and signal-to-noise ratio (SNR), which depend in turn on the performance of the radiofrequency (RF) coil. As ultrahigh $\mathbf{B}_0$ fields (up to 9.4 T in whole-body systems, with 11.7 T approved for human research) are introduced to exploit higher SNR [1], birdcage coils, which at present are the standard clinical MRI volume coils, become inadequate as radiative losses, end effects, and inductance effects become important [2,3]. Partially enclosed cavity resonators [4,5] and microstrip resonators [2] have been introduced to overcome some of these limitations. Predicting optimal RF design characteristics also becomes more difficult at ultrahigh fields because most modeling techniques make approximations that fail as the operating wavelength approaches, or even becomes smaller than, characteristic human anatomical dimensions [6–8].

In this paper, we examine the gapped toroidal cavity resonator [9] as presented in a patent by Vaughan [10] and which has been used, for example, for human studies at 4.1 T at the University of Alabama at Birmingham (UAB) [11]. Its most significant advantages for ultrahigh field MRI, high Q and $\mathbf{B}_1$ field uniformity, have been demonstrated previously, operating at 175 MHz [12–16]. While it cannot be driven in quadrature, its high efficiency appears to compensate more than adequately for this limitation at high field. Its bulky configuration also limits its possible applications: if the extent and bulk of the gapped toroid can be reduced without significant distortion to the $\mathbf{B}_1$ field, it may find more general MRI applications. Having an analytic solution for the $\mathbf{B}_1$ field of the gapped toroid provides some of the information necessary to reconfigure the resonator to this end.

* Corresponding author. Fax: +1 615 322 0734.
E-mail address: edward.j.butterworth@vanderbilt.edu (E.J. Butterworth).

1090-7807/$ - see front matter © 2005 Elsevier Inc. All rights reserved.
doi:10.1016/j.jmr.2005.03.021

1.1. RF modeling and field computation in MRI

Mathematically modeling an MRI coil positioned in the bore of a magnet and electrically coupled to a sample is a sufficiently complex task to require an array of approximations and simplifications, the choice of which will profoundly influence the applicability of the model. Several approaches for modeling selected MRI coil configurations have appeared in the literature. These include both analytic solutions of the applicable equations with appropriate boundary conditions, and numerical techniques including finite elements and the method of moments, among others, to simulate the fields produced by a given distribution of sources. Although analytic solutions are hard to find for all but the most simple configurations, they have the advantage, unlike purely numerical solutions, of providing physical insight into the nature of the problem, important because many aspects of RF behavior germane to ultrahigh field MRI remain poorly understood [17, pp. 51–55;18, p. 167]. In addition, an analytic solution is often computationally advantageous over iterative methods, even if it serves to solve only one step of the problem. Sometimes it is advantageous to solve a simplified version of the problem analytically, for example, a coil without a sample or with a geometrically symmetric sample, afterwards extending the result to a realistic human sample using a numerical algorithm. Solutions of this kind, as well as fully analytic solutions, have appeared in the literature [6,19–21].

Early in the history of MRI coil development, Roméo and Hoult [22] derived a general field solution to Laplace's equation in terms of zonal harmonics. Cylindrical geometry was addressed by Foò et al. [18], who modeled the load, RF coil, and shield as three infinitely long coaxial cylinders. By thus ignoring end effects, they reduced the problem to two dimensions. This model permits transverse electric (TE) and transverse magnetic (TM) solutions in terms of Bessel functions, and thus is limited by the fact that most MRI volume coils resonate in transverse electromagnetic (TEM) mode, which cannot be sustained in simply connected regions such as hollow pipes. Nevertheless, they show how a two-dimensional technique can be applied to a geometry of constant cross-section if end effects can be neglected. Keltner et al. [23] computed the fields for a surface coil adjacent to a spherical load at high field using a multipole expansion in spherical Bessel functions. This approach was amplified by Liu and Crozier [24], using a human head model comprising seven concentric layers. A bilinear conformal transformation provided the first stage in the TEM mode solution developed by Crozier et al. [20]. For both unshielded and shielded birdcage coils, they mapped the two-dimensional cross-section of the resonator onto a plane in which all rungs of the birdcage are aligned with the real axis. The electrostatic potential on the transformed geometry is readily found, and is used as the basis for a numerical algorithm to calculate the current density on each rung. Finally, they compute **B** from the current density. Jin et al. [7] developed a numerical method using a biconjugate gradient algorithm for fields inside a realistic head model, noting that certain inaccuracies arise when a finite element model is used. Leifer [25] derived a complete analytic solution for the modes of a birdcage coil operating at relatively low MRI frequency. A mixture of analytic and numerical techniques was used by Alecci et al. [21] to model a load having internal structure within the coil. Another approach, justifiable on certain geometries, is the use of transmission line methods, performed by Cassidy et al. [26] and Bogdanov and Ludwig [27]. More recently, Chin et al. [28] have presented a thorough treatment of the birdcage coil using methods based on circuit concepts. These solutions use well-understood electromagnetic principles and mathematical techniques that can be made very detailed as well as very accurate. However, circuit theory is intrinsically approximate, and becomes increasingly inappropriate with increasing operating frequency. As the wavelength approaches human dimensions, adequate modeling requires that we begin directly with Maxwell's equations and make simplifying assumptions appropriate to the device being modeled.

We present here a purely analytic solution, using a method roughly analogous to that given by Crozier et al. [20] for the birdcage coil: we make the simplifying assumption that the resonator contains no sample and operates in TEM mode. There the problem can be solved on a two-dimensional cross-section, where the transverse magnetic field of a TEM resonator can be represented as a static field multiplied by a complex propagation factor. The static field is obtained from a potential found by solving the two-dimensional Laplace's equation on that plane. In accord with general usage, the italicized B represents the magnitude only of the magnetic field, and the boldface **B** the vector quantity.

The gapped toroid, shown in perspective in Fig. 1, is a multiply connected reentrant cavity resonator [29, p. 116] consisting of a pair of coaxial conducting cylinders driven across an azimuthal slit encircling the outer cylinder at the midpoint (or alternatively, by an inductive loop inserted between the cylinders [10]), and shorted at both ends, with a longitudinal gap for the insertion of the sample. This device is essentially a short-circuited section of a two-conductor transmission line [30, pp. 482–485;31, pp. 213–214;32, pp. 365–377 and 396–400;33, pp. 535–536] which can support standing TEM waves, in which the electric vector **E** and the magnetic vector **H** are perpendicular to each other as well as to the Poynting vector **S**. The outer and inner cylinders of the gapped toroid are the two conductors carrying

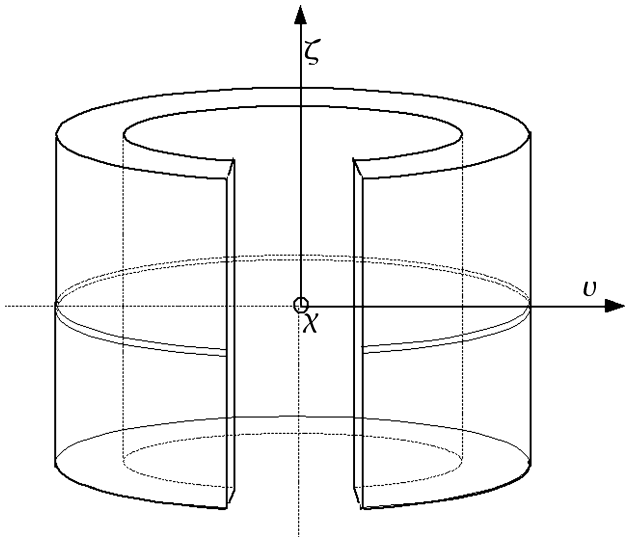

Fig. 1. Perspective view of the toroidal TEM resonator. We label the three-dimensional axes with the Greek letters χ, υ, and ζ to prevent confusion with the complex plane notation. In this view, the χ-axis is directed out of the paper toward the viewer.

oscillating current in opposite directions. The excitation current paths for this resonator are shown in Fig. 2.

This device is made self-resonant at the Larmor frequency by setting its overall axial length equal to one wavelength and driving it at the axial midpoint. The voltage is nulled at the two ends where the resonator is shorted, and hence another voltage null appears at its axial midplane. Voltage and current in the ideal

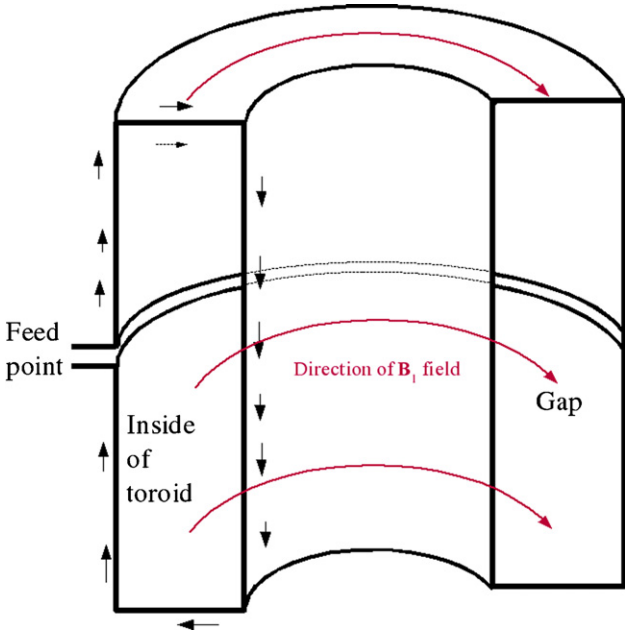

Fig. 2. A cross-section of the toroidal TEM resonator, showing the current paths. This resonator is best seen as a section of a two-conductor transmission line, shorted at both ends and driven at the midpoint. The gap providing sample access is seen to the right.

shorted resonator are out of phase by $\pi/2$, and the wave undergoes a π phase shift at each end of the resonator, thus the standing wave has maximum current (and hence maximum **B**-field amplitude) in the midplane. Each half of this resonator resembles the device pictured in [33, p. 536], with the input loop located at the point shown in position *A*.

A pure TEM mode is an idealization, since any practical device will excite some higher modes. In this device the **E** field near the driving point is not always transverse. However, the construction of the resonator and the voltage null in the midplane ensures that **E** is very small in that region. This condition, along with the standing wave pattern within the resonator (since the characteristic mode of operation of this resonator shape is the fundamental TEM_{00}, or cyclotron, mode), and the fact that the higher (non-TEM) modes have cutoff frequencies above those likely to be generated, guarantees that very little energy goes into these modes if the dimensions of the resonator are chosen carefully. We have not attempted to model these higher modes.

If the cross-section of a TEM resonator is uniform throughout its length in the direction of propagation (the ζ-direction in Fig. 1), then its **B** field has a simple relation to the potential of a static charge distribution on the same geometry. The **E** field of the latter is simply the gradient of the potential (from $\mathbf{E} = -\nabla\phi$). From the definition of the gradient, **E** is always directed perpendicular to the equipotential curves. Since **E** and **B** are perpendicular to each other on any transverse plane in a TEM wave, it follows that the **B** field produced when the static charge is replaced by a current flowing perpendicular to the plane must be directed *along* that equipotential curve. Because every magnetic field is divergence-free (or solenoidal; since $\nabla \cdot \mathbf{B} = 0$) the contours of *B* form closed loops about the current source which are congruent with the equipotentials. Thus, the static solution also gives the contours of *B*, and the length of any such contour may be found by integration and used to compute the magnitude of *B* via Ampère's law, while the direction of **B** is always along the path of that contour.

This approach is justified by considering the characteristics of purely harmonic propagation. If we define, as in Fig. 1, a three-dimensional right-handed Cartesian coordinate system (χ, υ, ζ) in which the wave propagates in the ζ-direction, Maxwell's equations reduce to the Heaviside equations

$$\left[\frac{\partial^2}{\partial\zeta^2} + j\omega\mu(\sigma + j\omega\varepsilon)\right]\begin{pmatrix}\mathbf{E_T}\\ \mathbf{H_T}\end{pmatrix} = 0, \tag{1}$$

where μ is the magnetic permeability in the constitutive relation $\mathbf{B} = \mu\mathbf{H}$, ω is angular frequency, σ the electrical conductivity, ε the permittivity, and the subscript (T) indicates that the field vectors are transverse to the direction of propagation and thus in the $\chi\upsilon$-plane. We use Greek letters for the coordinate axes to avoid

confusion with the letters designating the complex planes as introduced below. Eq. (1) have the solutions

$$\begin{pmatrix} \mathbf{E_T} \\ \mathbf{H_T} \end{pmatrix} = \begin{pmatrix} \mathbf{E_T^0} \\ \mathbf{H_T^0} \end{pmatrix} e^{-j\zeta\sqrt{j\omega\mu(\sigma+j\omega\varepsilon)}} e^{j\omega t} \equiv \begin{pmatrix} \mathbf{E_T^0} \\ \mathbf{H_T^0} \end{pmatrix} e^{-j(\gamma\zeta-\omega t)}, \tag{2}$$

where γ is the complex propagation constant. The $\mathbf{B}_1$ field then is

$$\mathbf{B}_1 = \mu \mathbf{H}_T^0 e^{-j(\gamma\zeta-\omega t)} \equiv \mathbf{B}_{1,0} e^{-j(\gamma\zeta-\omega t)}. \tag{3}$$

The $\mathbf{B}_{1,0}$ field is identical to that produced by steady currents in the conducting surfaces of the resonator, and the factor $e^{-j(\gamma\zeta-\omega t)}$ indicates the harmonic dependence on ζ and t. Note that for lossless media γ reduces to the wave number $k = \omega\sqrt{\mu\varepsilon}$.

2. Constructing the transforms

2.1. Physical representation

We define a complex z-plane (where $z = x + jy$) normal to the ζ-axis on which to model the physical geometry. The gapped toroid is represented on z by two concentric gapped circles (Fig. 3, top) representing the cross-sections of the cylinders, of outer radius R_2 and inner radius R_1. Computations are simplified by replacing these physical radii with dimensionless radii r_1 and r_2, where $R_1/r_1 = R_2/r_2$ and where the geometric mean of r_2 and r_1 is set to unity:

$$r_0 = \sqrt{r_1 r_2} \equiv 1. \tag{4}$$

The locus of points $r = r_0$ (a unit circle on z) represents the radial distance (located between the two gapped circles) at which the electric potential is zero when the potentials on the gapped circles are equal and opposite. Actual dimensions are found by multiplying the normalized quantities by R_2/r_2 (or R_1/r_1) after the dimensionless calculations are completed.

The circular geometry of the problem suggests using complex polar coordinates on z:

$$\begin{aligned} x + jy &= re^{j\theta}, \\ x &= r\cos\theta, \\ y &= r\sin\theta. \end{aligned} \tag{5}$$

These equations can be inverted to obtain

$$\begin{aligned} r &= \sqrt{x^2 + y^2} \\ \theta &= \arctan\left(\frac{y}{x}\right). \end{aligned} \tag{6}$$

Since the gap has the same physical extent through both circles while the circles have different diameters (see Fig. 3, top), the gap in the inner circle subtends a larger angle (θ_1) as measured from the x-axis than that in the outer circle (θ_2). The physical distance from the x-axis

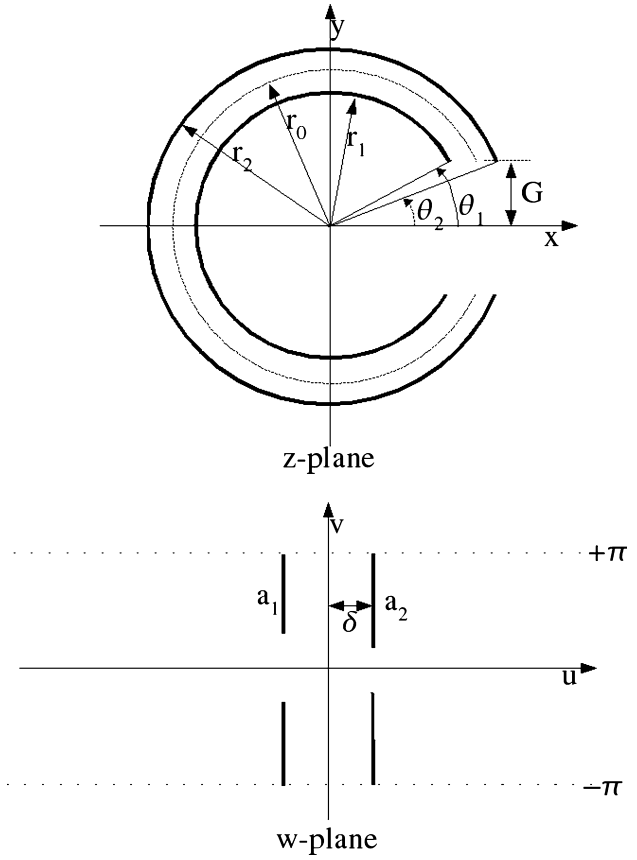

Fig. 3. The two complex planes used for the conformal transformation. At top is the z-plane on which the physical geometry is represented; at bottom the rectangular w-plane to which it is mapped by the logarithmic transformation.

to the lip of the gap (the half-gap) is called G (see Fig. 3), and a dimensionless ratio g gives the relative size of this half-gap as

$$g = \frac{G}{R_2} \tag{7}$$

in terms of which θ_1 and θ_2 are given by

$$\begin{aligned} \theta_1 &= \arcsin\left(g\frac{r_2}{r_1}\right), \\ \theta_2 &= \arcsin(g). \end{aligned} \tag{8}$$

2.2. The logarithmic transform

We now introduce a w-plane (where $w = u + jv$) to which the physical geometry on z is mapped using the logarithmic transform given by

$$\begin{aligned} w &= \ln z, \\ u &= \ln\sqrt{x^2 + y^2}, \\ v &= \arctan\left(\frac{y}{x}\right). \end{aligned} \tag{9}$$

The solution found on w is transformed back to z with the inverse (exponential) transform

$$z = e^{w},$$
$$x = e^{u}\cos v. \tag{10}$$
$$y = e^{u}\sin v.$$

In terms of the radial coordinates of Eqs. (6) and (9) become

$$u = \ln r,$$
$$v = \theta - \pi. \tag{11}$$

Due to the periodicity of the azimuthal component, the logarithmic transform maps the entire z-plane to a strip on the interval $u = [-\infty, +\infty]$, $v = [-\pi, +\pi]$ on w, mapping all circles concentric about the origin on z to vertical line segments on $[-\pi, +\pi]$. The unit circle is mapped to the v-axis ($u = 0$), larger circles to $u > 0$ and smaller circles to $u < 0$. The advantage of normalizing the geometric mean of r_1 and r_2 to unity (Eq. (4)) is now apparent: the circle of radius r_0 maps to the v-axis, and the two circles on z are mapped to two vertical line segments positioned symmetrically about the v-axis on w, offset from $u = 0$ by normalized lengths $u = \pm\delta$, given by

$$\delta = \frac{1}{2}\ln\frac{r_2}{r_1}. \tag{12}$$

Likewise, the angular gaps in the cylinders on z are mapped to gaps in the vertical line segments on w. From Eq. (11), the angular measure of any arc on z (in radians) is numerically equal to the dimensionless vertical length to which it is mapped on w, i.e., an arc of $\pi/4$ as measured from the x-axis on z transforms to a line segment of height $\pi/4$ on w, and a complete circle on z maps to a vertical line from $-\pi$ to $+\pi$ on w, the radius of the circle being represented by the u-coordinate.

The definition of the angle θ on z is also chosen to simplify computation on w. Since the logarithmic transform maps the $-x$-axis on z to the two discontinuous boundaries at $v = \pm\pi$ on w, and the gap in the toroid is the region of interest, we define θ so that the transform will map the region opposite the gap on z to the infinities, displacing any discontinuity artifacts to points far removed from the region of interest. This is implemented by using $v = \theta - \pi$ rather than the straightforward $v = \theta$ in Eq. (11), thus setting θ at $-\pi$ on the $-x$-axis, from whence it increases as it traverses the plane in a counterclockwise direction, reaching zero on the $+x$-axis, and terminating at $+\pi$ as it returns to the $-x$-axis. This choice has the effect of positioning the gaps symmetrically about the $+x$-axis on z, so that they will be mapped to the region about the w-origin (see Fig. 3, bottom), while the discontinuity at $v = \pm\pi$ then represents the region of the toroid opposite to the gap.

With these definitions, this transformation maps each arc to a pair of vertically collinear segments separated by a gap about $v = 0$. The $+x$-axis is transformed to the entire u-axis ($v = 0$), and the negative $-x$-axis to the discontinuous boundaries at $v = \pm\pi$. In effect, the z-plane is broken along the $-x$-axis to map the gap to the central region on w, as if the w-plane that would have resulted from a $v = \theta$ transform were cut along the u-axis and the top and bottom halves transposed. The periodic nature of this transform permits another visualization: since the entire pattern repeats with a period of 2π in the v-direction, the transpose can alternatively be regarded as the center region of a wider plane ranging from -2π to $+2\pi$ in which the region from 0 to $+2\pi$ exactly replicates the region from -2π to 0.

The lengths of the segments to which the arcs are transformed (a_1, a_2) are given by

$$a_1 = \pi - \theta_1,$$
$$a_2 = \pi - \theta_2. \tag{13}$$

Because the mapping is conformal, equipotential curves about these segments map to equipotential curves about the circular arcs when the transform is inverted.

2.3. Elliptical coordinates

The equipotentials of a line segment take the form of a family of confocal ellipses (Fig. 4), the endpoints being the common foci. This suggests introducing elliptical coordinates [34] on w, where the radial coordinate η and azimuthal coordinate ψ are defined by the equations

$$u = a\sinh\eta\sin\psi,$$
$$v = a\cosh\eta\cos\psi. \tag{14}$$

where $2a$ is the distance between the common foci. The line segment is a degenerate ellipse ($\varepsilon = 1$, $\eta = 0$), and all

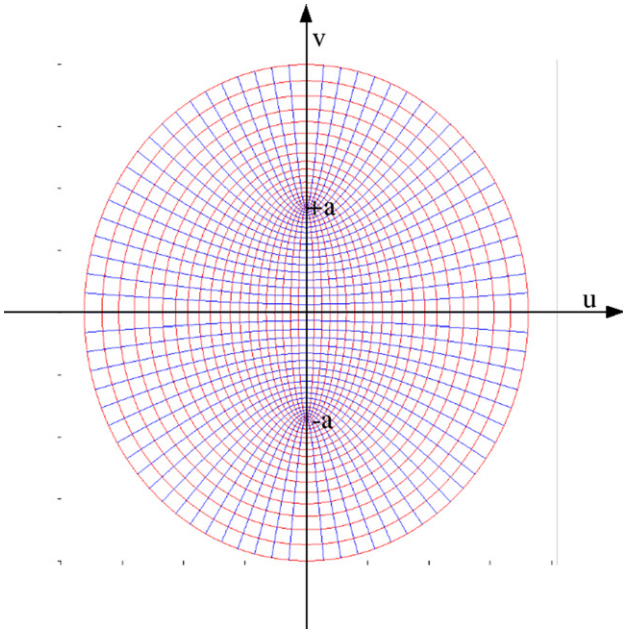

Fig. 4. The family of confocal ellipses and hyperbolae around the segment $\eta = 0$.

values $\eta > 0$ represent ellipses of increasing size and decreasing eccentricity ($\varepsilon = \operatorname{sech}\eta$). These confocal ellipses are also the level curves of B about a current flowing in that segment perpendicular to the plane. Since each ellipse encloses the current source and the magnitude of B is constant around any confocal ellipse, B is found from Ampere's law after calculating the arc length around the ellipse (an elliptic integral).

The transposition of the top and bottom halves of w described also transposes the equipotential curves. For each set of ellipses, this transposition is best visualized by cutting Fig. 4 along the x-axis and transposing the top and bottom halves. The line segments a_1 and a_2 to which the two arcs transform are thus the common focal distances from the transposed origins for the two families of ellipses. About these four segments are four sets of half-ellipses in $\eta_i (i = 1,2,3,4)$, as shown in Fig. 5. Inverting Eq. (14) gives these η_i as functions of u and v. We show here the inversion of η_1, the other inversions being easily obtained by the proper sign changes. Since the magnitude of B is a function only of the η_i we eliminate ψ_i from the elliptical equations, yielding

$$\left(\frac{u-\delta}{\sinh\eta_1}\right)^2 + \left(\frac{v-\pi}{\cosh\eta_1}\right)^2 = a_2^2, \tag{15}$$

$$\left(\frac{u-\delta}{\sinh\eta_1}\right)^2 + \left(\frac{v+\pi}{\cosh\eta_1}\right)^2 = a_2^2, \tag{16}$$

$$\left(\frac{u+\delta}{\sinh\eta_1}\right)^2 + \left(\frac{v-\pi}{\cosh\eta_1}\right)^2 = a_1^2, \tag{17}$$

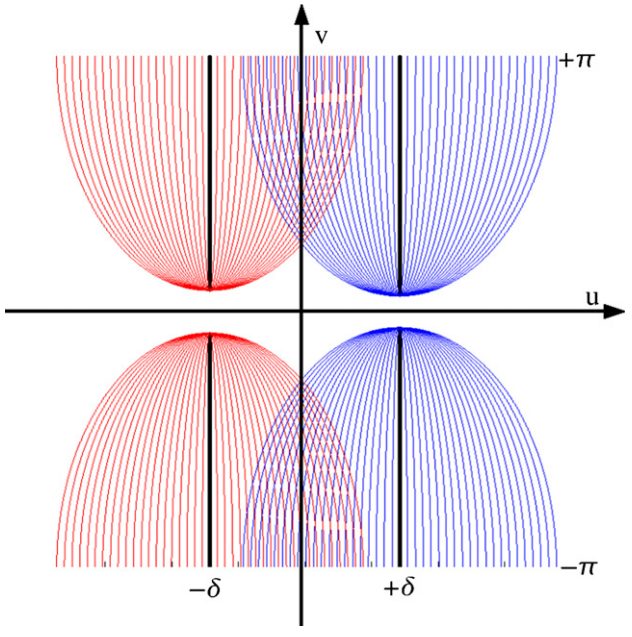

Fig. 5. The four sets of confocal ellipses around the four $\eta_i = 0$ half-strips. For clarity, only the lowest values of η are plotted. Note that horizontal distances are expanded.

$$\left(\frac{u+\delta}{\sinh\eta_1}\right)^2 + \left(\frac{v+\pi}{\cosh\eta_1}\right)^2 = a_1^2. \tag{18}$$

After applying some trigonometric and hyperbolic identities [35] and invoking the quadratic formula, we obtain

$$\eta_1 = \frac{1}{2}\operatorname{arccosh}\left\{\frac{(u-\delta)^2 + (v-\pi)^2}{a_2^2} + \sqrt{\left[\frac{(u-\delta)^2 + (v-\pi)^2}{a_2^2} - 1\right]^2 + \frac{4(u-\delta)^2}{a_2^2}}\right\}. \tag{19}$$

For **B** as a function of any point (x, y), we substitute for u and v in the above from Eq. (10); for $\mathbf{B}(r,\theta)$, from Eq. (13).

3. Computing the magnetic field

3.1. Calculation of curve length

If the length of a level curve of B is known, the magnitude of B on that curve is found from Ampere's circuital law in the simplified form

$$B = \frac{\mu I}{L}, \tag{20}$$

where L is the closed curve length. That length is found by parametrizing the curve by ψ while holding η constant and integrating the arc length formula

$$L = \int_0^{2\pi} \sqrt{\left(\frac{\partial x}{\partial \psi}\right)^2 + \left(\frac{\partial y}{\partial \psi}\right)^2}\, d\psi. \tag{21}$$

Since x and y as functions of u and v, this integral expands to

$$L = \int_0^{2\pi} \sqrt{\left(\frac{\partial x}{\partial u}\frac{\partial u}{\partial \psi} + \frac{\partial x}{\partial v}\frac{\partial v}{\partial \psi}\right)^2 + \left(\frac{\partial y}{\partial u}\frac{\partial u}{\partial \psi} + \frac{\partial y}{\partial v}\frac{\partial v}{\partial \psi}\right)^2}\, d\psi. \tag{22}$$

To evaluate it, we calculate the derivatives of u and v with respect to ψ:

$$\begin{aligned} \frac{\partial u}{\partial \psi} &= a\sinh\eta\cos\psi, \\ \frac{\partial v}{\partial \psi} &= -a\cosh\eta\sin\psi. \end{aligned} \tag{23}$$

Substituting from Eq. (10) gives the derivatives of x and y with respect to u and v:

$$\begin{aligned} \frac{\partial x}{\partial u} &= \frac{\partial}{\partial u}(e^u\cos v) = e^u\cos v = x, \\ \frac{\partial x}{\partial v} &= \frac{\partial}{\partial v}(e^u\cos v) = -e^u\sin v = -y, \\ \frac{\partial y}{\partial u} &= \frac{\partial}{\partial u}(e^u\sin v) = e^u\sin v = y, \\ \frac{\partial y}{\partial v} &= \frac{\partial}{\partial v}(e^u\sin v) = e^u\cos v = x \end{aligned} \tag{24}$$

as required by the Cauchy–Riemann conditions. Substituting Eqs. (23) and (24) into (22) and invoking the appropriate trigonometric and hyperbolic identities, we obtain

$$L(\eta) = a\int_0^{2\pi} e^{a\sinh\eta\sin\psi}\sqrt{(\sinh^2\eta+\sin^2\psi)}\,d\psi \tag{25}$$

This is the transformation of the elliptic integral, as it gives the arc length around a curve formed by an ellipse under an exponential transformation. To account for both arcs we substitute a_1 and a_2 for a:

$$\begin{aligned} L_1(\eta) &= a_1\int_0^{2\pi} e^{a_1\sinh\eta\sin\psi}\sqrt{(\sinh^2\eta+\sin^2\psi)}\,d\psi \\ L_2(\eta) &= a_2\int_0^{2\pi} e^{a_2\sinh\eta\sin\psi}\sqrt{(\sinh^2\eta+\sin^2\psi)}\,d\psi \end{aligned} \tag{26}$$

Thus L, from which B is determined, is a function only of η. Since there is no known evaluation of this integral in terms of elementary functions, it must be integrated numerically. The physical length is recovered from the normalized values used above by multiplying the L_i by R_2/r_2, as described above.

3.2. Resolving the field into rectangular components

The two arcs represent cross-sections of cylinders carrying currents in opposite directions, each producing its own magnetic field. The $\mathbf{B}_1$ field is the vector sum of these two fields, and is found by resolving each field into components (either r–θ or x–y components on z), and adding them componentwise. On each family of curves, $\mathbf{B}$ is found by multiplying the L_i (Eq. (26)) by R_2/r_2, as indicated above, and substituting into Ampere's law (Eq. (20)), yielding four overlapping sets of contours, reducible to two by reflective symmetry about the u-axis. Because the mapping is conformal (preservation of angles), the angle between any pair of intersecting curves on w must equal that between the images of those curves at the corresponding point on z. Thus the angle at which the level η-curve intersects a u-parallel on w at any point w_0 must equal that at which the curve on z to which the η-curve is transformed intersects a radial line at the point z_0 to which w_0 is transformed. This angle, called ξ, is given by

$$\xi_1 = \arctan\left(-\frac{u-\delta}{v-\pi}\coth^2\eta_1\right) \tag{27}$$

and, with the proper sign changes of δ and π, for the other families of η_i curves. The x and y components of $B_i (i = 1,\ldots,4)$ are then given by:

$$\begin{aligned} B_{x,i} &= B_i\cos\xi_i, \\ B_{y,i} &= B_i\sin\xi_i. \end{aligned} \tag{28}$$

The $\mathbf{B}$ field is found by summation:

$$\mathbf{B} = B_x\,\hat{\mathbf{x}} + B_y\,\hat{\mathbf{y}} = \hat{\mathbf{x}}\sum_1^4 B_{x,i} + \hat{\mathbf{y}}\sum_1^4 B_{y,i} \tag{29}$$

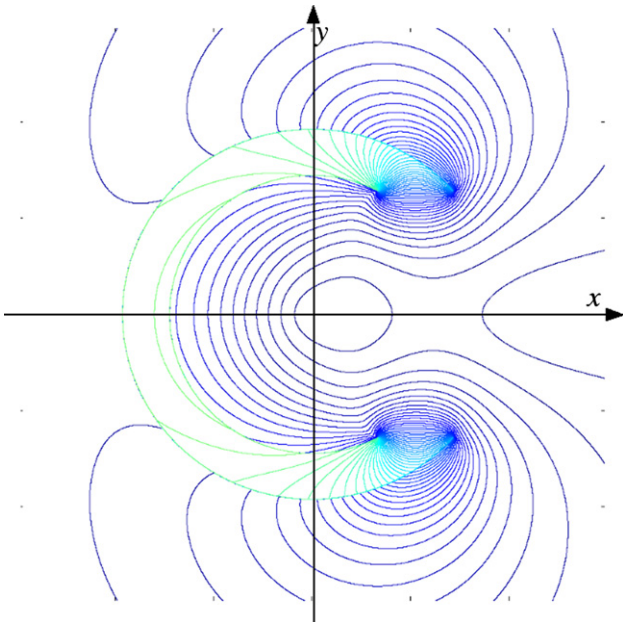

Fig. 6. Contours of constant B_1 magnitude on the gapped toroid cross-section. Note the artifactual hot spot at the back of the coil. Each contour represents a change of 2% in field strength.

where $\hat{\mathbf{x}}$ and $\hat{\mathbf{y}}$ are dimensionless rectangular unit vectors. The level curves of the resultant $\mathbf{B}$ field on z are shown in Fig. 6. Finally, the MRI-relevant standing wave field is given by

$$\mathbf{B}_1 = \mathbf{B}e^{-j(\gamma\zeta-\omega t)}, \tag{30}$$

where the ζ-coordinate represents the direction of propagation. Note that this analysis could in principle have been performed using r-θ coordinates on z.

4. Results

We have implemented this solution in MATLAB and FORTRAN (code available on request), using the diameter of the outer cylinder, aspect ratio, gap size, current, and the resolution of the computational grid as input parameters. The output is the magnitude and direction of the $\mathbf{B}_1$ field at every point in the cross-sectional plane. The TEM condition is maintained as long as the separation between the two cylinders is not large enough to represent a significant fraction of a wavelength. Input parameters may be varied to investigate the effects on $\mathbf{B}_1$ strength and homogeneity in the region of interest. As long as the field is essentially TEM and the length of the center-fed resonator equal to one wavelength, the above solution need only be multiplied by $e^{-j(\gamma\zeta-\omega t)}$ (Eq. (3)) to obtain the time-varying field. It is then possible to integrate over the field in the entire plane to compute the oscillating power through the plane, and from that the average energy density stored in the field.

The Fortran routine written for this study was run on a 1000×1000 grid on an Athlon64 machine in under three minutes, and Fig. 6 was produced with a massive 6000×6000 grid that required about an hour to run.

Our results are consistent with previously published experimental results [9–11], showing that the resonator establishes a near-homogeneous $\mathbf{B}_1$ field in the region of the gap. The contours in Fig. 6 represent increments of 2% in field magnitude. Repeated runs while varying the parameters have shown that a relatively uniform field can be produced even with a relatively large gap and aspect ratio. The computation shows, in addition, that the field is very small even at moderate distances from the resonator: there is no need to compute the fields beyond a normalized distance of 1.8 from the origin. As expected, the field diverges somewhat more rapidly for large gap and small aspect ratio. By integrating over the slice in which $\mathbf{B}_1$ was computed, we determined the energy stored in that field, and by comparing the energy in the entire plane with that in the annulus between R_1 and R_2 we found that for almost every reasonable combination of gap size and aspect ratio, about 90% of the magnetic field energy is stored in the region of interest between R_1 and R_2. This behavior is a consequence of the confinement of the EM energy in this coil design, where the resonating volume outside the sample is almost completely enclosed by the conducting surfaces, allowing very little energy to be radiated away. This is particularly important at high fields where every exposed conductor, being a significant fraction of a wavelength, behaves as an antenna and radiative losses quickly become significant.

5. Discussion, applications, and future directions

The gapped toroid has several characteristics that suit it uniquely for ultrahigh field MRI. The near-complete enclosure of the resonating volume minimizes radiative losses, giving the resonator an exceptionally high Q. Its current path is distributed over the entire cylindrical surface, minimizing resistive losses even at the small skin depths encountered at high frequencies. In addition, it is mechanically and electromagnetically simple: it does not require the networks of capacitors or inductors used in some RF coils, and does not generate the complex current patterns that these elements often produce. These characteristics make it a suitable starting point for future ultrahigh field designs.

We have presented an analytic solution for the $\mathbf{B}_1$ field of the gapped toroid, which is exact if the axial length is exactly equal to one wavelength and the arcs are perfectly circular cylinders. Modeling ideal performance is straightforward but can neither account directly for imperfections nor quantify the relation between degree of imperfection and effect on performance. Thus, it confirms the high performance available from the gapped toroid design, but serves only minimally as a guide to improving it. Nevertheless, it is the basis for advanced designs, and the Vaughan patent suggests several possible alterations to the basic design for further performance improvements. These include changes to the shape of the cylindrical cross-section, changes to the gap aperture that include partial enclosure, and filling the resonating volume with dielectric material. Using the present algorithm we have modified the gapped toroid by substituting a collapsed structure for the inner cylinder (Fig. 7). The resulting $\mathbf{B}_1$ field may be acceptable for some applications, but is not ideally homogeneous. While graphical methods may in principle extend the application of this algorithm [30, pp. 86–93], a solution is not obtained merely by "flattening" the cross-section using a computer graphics program, since this procedure does not preserve angles. We are investigating a toroid of elliptical cross-section, by analogy with an elliptical birdcage [20,36], using an elliptical conformal transform based on the elliptical coordinate system [34], in which the ellipses are transformed to a rectangular system on which the field solution is obtained. Similarly, a Cassinian oval cross-section may be derived [34, pp. 52 and 62;37,38].

To investigate the advantages of greater enclosure, we have introduced a toroid consisting of two complete cylinders, the sample aperture being reduced to a circular or oval hole cut through both cylinders. As expected, this altered configuration reduces power consumption

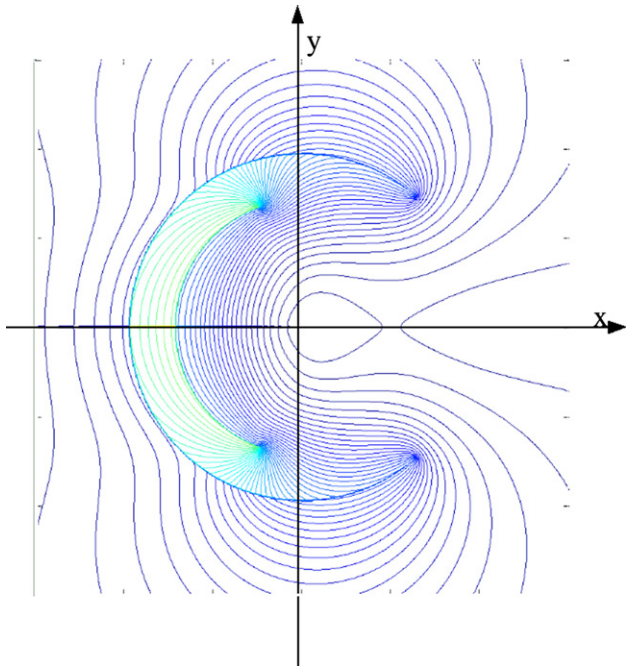

Fig. 7. Contours of constant B_1 magnitude on a somewhat distorted gapped toroid. Each contour represents a change of 2% in field strength.

still further [11] but further restricts sample access. Head, ankle, and breast images have been obtained with this coil. Another possible improvement, dielectric filling in the gapped toroid, was suggested in the Vaughan patent [10] and implemented by one of the authors [11] using powdered titanium dioxide (TiO_2) in rutile form. This resonator used considerably less RF power than comparable devices, due to the reduction of the reflection coefficient at the interface with human tissue [30, pp. 382–388;39, pp. 278–282].

Finally, it is necessary to model the human body in the coil under MRI conditions. The electrical properties of human tissue are known [40] and numerical models of the head and other body parts are now available [24,41–44]. These models can be incorporated into a simulation of the toroidal resonator used with the anatomy of interest. We have found an analytic solution to the problem of a homogeneous sphere in a uniform EM field [45], assuming the radius of the sphere to be larger than the EM wavelength within the sphere (consistent with the highest fields now under consideration), and will use this to develop a model of the resonator containing a human head.

References

[1] M. Takahashi, H. Uematsu, H. Hatabu, MR imaging at high magnetic fields, Eur. J. Radiol. 46 (2003) 45–52.

[2] X. Zhang, K. Ugurbil, W. Chen, A microstrip transmission line volume coil for human head MR imaging at 4 T, J. Magn. Reson. 161 (2003) 242–251.

[3] J.T. Vaughan, G. Adriany, C.J. Snyder, J. Tian, T. Thiel, L. Bolinger, H. Liu, L. DelaBarre, K. Ugurbil, Efficient high-frequency body coil for high-field MRI, Magn. Reson. Med. 52 (2004) 851–859.

[4] K. Woelk, J.W. Rathke, R.J. Klinger, The toroidal cavity NMR detector, J. Magn. Reson. A 109 (1994) 137–146.

[5] J.T. Vaughan, H.P. Hetherington, J.O. Otu, J.W. Pan, G.M. Pohost, High frequency volume coils for clinical NMR imaging and spectroscopy, Magn. Reson. Med. 32 (1994) 206–218.

[6] C. Mahony, L.K. Forbes, S. Crozier, D.M. Doddrell, A novel approach to the calculation of RF magnetic and electric fields for NMR coils of arbitrary geometry, J. Magn. Reson. B 107 (1995) 145–151.

[7] J.M. Jin, J. Chen, W.C. Chew, H. Gan, R.L. Magin, P.J. Dimbylow, Computation of electromagnetic fields for high-frequency magnetic resonance imaging applications, Phys. Med. Biol. 41 (1996) 2719–2738.

[8] M.D. Harpen, Cylindrical coils near self-resonance, Magn. Reson. Med. 30 (1993) 489–493.

[9] J.T. Vaughan, H.P. Hetherington, G.M. Pohost, A toroidal cavity coil for high-frequency clinical NMR, in: Proceedings of the third Meeting, *SMRM*, Nice, France, 1995, p. 996.

[10] J.T. Vaughan, Cavity resonator for NMR systems, US Patent 5,744,957 (1998).

[11] E.J. Butterworth, E.G. Walsh, J.W. Hugg, A TiO_2 dielectric filled toroidal radio frequency cavity resonator for high field NMR, NMR Biomed. 14 (2001) 1–8.

[12] H.P. Hetherington, J.W. Pan, W.J. Chu, G.F. Mason, B.R. Newcomer, Biological and clinical MRS at ultra-high field, NMR Biomed. 10 (8) (1997) 360–371.

[13] M.M. Bamman, B.R. Newcomer, D.E. Larson-Meyer, R.L. Weinsier, G.R. Hunter, Evaluation of the strength-size relationship in vivo using various muscle size indices, Med. Sci. Sports Exerc. 32 (7) (2000) 1307–1313.

[14] D.E. Larson-Meyer, B.R. Newcomer, G.R. Hunter, H.P. Hetherington, R.L. Weinsier, 31P MRS measurement of mitochondrial function in skeletal muscle: reliability, force-level sensitivity and relation to whole body maximal oxygen uptake, NMR Biomed. 13 (1) (2000) 14–27.

[15] D.E. Larson-Meyer, B.R. Newcomer, G.R. Hunter, J.E. McLean, H.P. Hetherington, R.L. Weinsier, Effect of weight reduction, obesity predisposition, and aerobic fitness on skeletal muscle mitochondrial function, Am. J. Physiol. Endocrinol. Metab. 278 (1) (2000) E153–E161.

[16] G.R. Hunter, B.R. Newcomer, R.L. Weinsier, D.L. Karapondo, D.E. Larson-Meyer, D.R. Joanisse, M.M. Bamman, Age is independently related to muscle metabolic capacity in premenopausal women, J. Appl. Physiol. 93 (1) (2002) 70–76.

[17] C.M. Collins, S. Li, Q.X. Yang, M.B. Smith, A method for accurate calculation of $\mathbf{B}_1$ fields in three dimensions. Effects of shield geometry on field strength and homogeneity in the birdcage coil, J. Magn. Reson. 125 (1997) 233–241.

[18] T.K.F. Foò, C.E. Hayes, Y.-W. Kang, An analytic model for the design of RF resonators for MR body imaging, Magn. Reson. Med. 21 (1991) 165–177.

[19] G. Giovanetti, L. Landini, M.F. Santarelli, V. Positano, A fast and accurate simulator for the design of birdcage coils in MRI, MAG'MA 15 (2002) 36–44.

[20] S. Crozier, L.K. Forbes, W.U. Roffmann, K. Luescher, D.M. Doddrell, A methodology for current density calculations in high frequency RF resonators, Concepts Magn. Reson. 9 (1997) 195–210.

[21] M. Alecci, C.M. Collins, M.B. Smith, P. Jezzard, Radio frequency magnetic field mapping of a 3 Tesla birdcage coil: experimental and theoretical dependence on sample properties, Magn. Reson. Med. 46 (2001) 379–385.

[22] F. Roméo, D.I. Hoult, Magnet field profiling: analysis and correcting coil design, Magn. Reson. Med. 1 (1984) 44–65.

[23] J.R. Keltner, J.W. Carlson, M.S. Roos, S.T.S. Wong, T.L. Wong, T.F. Budinger, Electromagnetic fields of surface coils in vivo NMR at high frequencies, Magn. Reson. Med. 22 (1991) 467–480.

[24] F. Liu, S. Crozier, Electromagnetic fields inside a lossy, multilayered spherical head phantom excited by MRI coils: models and methods, Phys. Med. Biol. 49 (2004) 1835–1851.

[25] M.C. Leifer, Resonant modes of the birdcage coil, J. Magn. Reson. 124 (1997) 51–60.

[26] P.J. Cassidy, S. Grieve, K. Clarke, D.J. Edwards, Electromagnetic characterization of MR RF coils using the transmission-line method, MAG'MA 14 (2002) 20–29.

[27] G. Bogdanov, R. Ludwig, Coupled microstrip line transverse electromagnetic resonator model for high-field magnetic resonance imaging, Magn. Reson. Med. 47 (2002) 579–593.

[28] C.-H. Chin, C.M. Collins, S. Li, B.J. Dardzinski, M.B. Smith, Birdcage builder: design of specified-geometry birdcage coils with desired current pattern and resonant frequency, Concepts Magn. Reson. 15 (2002) 156–163.

[29] R. Müller, Theory of cavity resonators, in: G. Goubau (Ed.), Electronic Waveguides and Cavities, Pergamon Press, Oxford, 1961.

[30] J.D. Kraus, K.R. Carver, Electromagnetics, McGraw-Hill, New York, 1973.

[31] G. Montgomery, R.H. Dicke, E.M. Purcell, Principles of Microwave Circuits, McGraw-Hill, New York, 1947.

[32] U.S. Inan, A.S. Inan, Electromagnetic Waves, Prentice-Hall, Upper Saddle River, NJ, 2000.

[33] S. Ramo, J.R. Whinnery, T. van Duzer, Fields and Waves in Communication Electronics, Wiley, New York, 1965.

[34] P. Moon, D.E. Spencer, Field Theory Handbook, Including Coordinate Systems, Differential Equations and Their Solutions, Springer-Verlag, Berlin, 1971.
[35] M. Abrahamowitz, I. Stegun (Eds.), Handbook of Mathematical Functions with Formulas, Graphs, and Mathematical Tables. First Published by National Bureau of Standards, 1964, Dover, New York, 1972.
[36] N. De Zanche, P.S. Allen, Sensitivity calculations and comparisons for shielded elliptical and circular birdcage coils, Magn. Reson. Med. 47 (2002) 364–371.
[37] P.S. Allen, N. De Zanche, Nuclear magnetic resonance birdcage coil with Cassinian oval former, US Patent 6,452,393 (2002).
[38] N. De Zanche, A. Yahya, F.E. Vermeulen, P.S. Allen, Analytical approach to noncircular section birdcage coil design: verification with a Cassinian oval coil, Magn. Reson. Med. 53 (2005) 201–211.
[39] J.D. Jackson, Classical Electrodynamics, second ed., Wiley, New York, 1975.
[40] S. Gabriel, R.W. Lau, C. Gabriel, The dielectric properties of biological tissues II: measurements in the frequency range 10 Hz to 20 GHz; III: parametric models for the dielectric spectrum of tissues, Phys. Med. Biol. 41 (1996) 2271–2293.
[41] J.G. Harrison, J.T. Vaughan, Finite element modeling of head coils for high-frequency magnetic resonance applications, in: 12th Annu. Rev. Prog. Appl. Compu. Electromag., 1996, pp. 1220–1226.
[42] A. Drossos, The dependence of electromagnetic energy absorption upon human head tissue composition in the frequency range of 3000-3000 MHz, IEEE Trans. Microwave Theory Tech. 48 (2000) 1988–1995.
[43] L. Spinelli, S.G. Andino, G. Lantz, M. Seech, C.M. Michel, Electromagnetic inverse solutions in anatomically constrained spherical head models, Brain Topogr. 13 (2000) 115–125.
[44] http://www.nlm.nih.gov/research/visible/visible_human.html.
[45] E.J. Butterworth, Computation of reflection/refraction from the human head in high-field MRI, in: Annual conference, Southeast Section, American Physical Society, 2004, BB.003.